

# Agglomeration of Non-metallic Inclusions at Steel/Ar Interface: *In-Situ* Observation Experiments and Model Validation



WANGZHONG MU, NESLIHAN DOGAN, and KENNETH S. COLEY

Better understanding of agglomeration behavior of nonmetallic inclusions in the steelmaking process is important to control the cleanliness of the steel. In this work, a revision on the Paunov simplified model has been made according to the original Kralchevsky–Paunov model. Thus, this model has been applied to quantitatively calculate the attractive capillary force on inclusions agglomerating at the liquid steel/gas interface. Moreover, the agglomeration behavior of  $\text{Al}_2\text{O}_3$  inclusions at a low carbon steel/Ar interface has been observed *in situ* by high-temperature confocal laser scanning microscopy (CLSM). The velocity and acceleration of inclusions and attractive forces between  $\text{Al}_2\text{O}_3$  inclusions of various sizes were calculated based on the CLSM video. The results calculated using the revised model offered a reasonable fit with the present experimental data for different inclusion sizes. Moreover, a quantitative comparison was made between calculations using the equivalent radius of a circle and those using the effective radius. It was found that the calculated capillary force using equivalent radius offered a better fit with the present experimental data because of the inclusion characteristics. Comparing these results with other studies in the literature allowed the authors to conclude that when applied in capillary force calculations, the equivalent radius is more suitable for inclusions with large size and irregular shape, and the effective radius is more appropriate for inclusions with small size or a large shape factor. Using this model, the effect of inclusion size on attractive capillary force has been investigated, demonstrating that larger inclusions are more strongly attracted.

DOI: 10.1007/s11663-017-1027-4

© The Minerals, Metals & Materials Society and ASM International 2017

## I. INTRODUCTION

IT is well known that the control of the nonmetallic inclusions in steel is vital due to the increasing demands of high-quality steel grades. Steelmakers aim to produce steel with less inclusions in order to reduce nozzle clogging during continuous casting and improve mechanical properties in the final product.<sup>[1,2]</sup> The concept of inclusion engineering has been applied in the field of ferrous process metallurgy.<sup>[3]</sup> This concept deals with the control of the amount, morphology, size distribution, and composition of nonmetallic inclusions formed in liquid metal during refining and solidification. Moreover, argon bubbling is considered as an important method for removing nonmetallic inclusions from liquid

steel,<sup>[4]</sup> because the flotation of inclusions is enhanced by adherence to bubbles. Moreover, argon bubbling can create turbulent eddy flow from bath stirring, which improves inclusion agglomeration.<sup>[5–7]</sup> Therefore, the agglomeration behavior of nonmetallic inclusions at the steel/Ar interface needs to be well understood and controlled. While the authors are aware that there are a number of mechanisms that are important in the agglomeration of inclusions,<sup>[8–14]</sup> the focus of the current work is entirely aimed at the agglomeration of inclusions at metal/gas interfaces. This is relevant to interaction between inclusions and bubbles, is necessary to understand observed inclusion behavior in the confocal laser scanning microscopy (CLSM), and has the potential to offer important insights into inclusion agglomeration at the slag/metal interface.

The collision and agglomeration of inclusions has been investigated experimentally by using high-temperature CLSM. The agglomeration of  $\text{Al}_2\text{O}_3$ ,<sup>[8,14]</sup> 80 pct  $\text{Al}_2\text{O}_3$ ·20 pct  $\text{SiO}_2$ ,<sup>[8]</sup>  $\text{CaO}$ · $\text{Al}_2\text{O}_3$  with different ratios of  $\text{Ca}/\text{Al}$ ,<sup>[9]</sup>  $\text{MgO}$ ,<sup>[10]</sup> 93 pct  $\text{Al}_2\text{O}_3$ ·7 pct  $\text{MgO}$ ,<sup>[10]</sup> complex  $\text{Al}_2\text{O}_3$ · $\text{CaO}$ · $\text{MgO}$  and  $\text{Al}_2\text{O}_3$ · $\text{CaO}$ · $\text{SiO}_2$ ,<sup>[11]</sup>  $\text{Al}_2\text{O}_3$ · $\text{Ce}_2\text{O}_3$ ,<sup>[12]</sup>  $\text{MgAl}_2\text{O}_4$ ,<sup>[14,15]</sup> and liquid inclusions<sup>[11,14]</sup> at the steel/Ar interface has been reported. Besides the

---

WANGZHONG MU, NESLIHAN DOGAN, and KENNETH S. COLEY are with the Department of Materials Science and Engineering, McMaster Steel Research Centre, McMaster University, 1280 Main Street West, Hamilton, ON L8S 4L7, Canada. Contact email: wangzhongmu@gmail.com

Manuscript submitted January 23, 2017.

Article published online July 24, 2017.

experimental works, Nakajima and co-workers<sup>[10,11]</sup> pioneered the application of the Kralchevsky–Paunov model<sup>[16,17]</sup> to process metallurgy, calculating the capillary force for inclusion agglomeration at the steel/Ar interface. However, the inclusions in their calculations are only defined as solid particle, liquid particle, and complex particle. The quantitative analysis for inclusions with different chemical compositions has not been made.

In this work, the attractive forces between agglomerating Al<sub>2</sub>O<sub>3</sub> inclusions with various sizes were measured *in situ* by CLSM; thereafter, the experimental results were compared with the calculations by the revised Kralchevsky–Paunov model. The effect of inclusion size on attractive capillary force was investigated by using this model. In addition, the bending behavior of inclusions agglomerating at the steel/Ar interface was investigated.

## II. METHODOLOGY

### A. Experiments

The chemical composition of steel used in this work is shown in Table I. High-temperature CLSM (Lasertec VL2000DX) using a He–Ne laser together with an infrared image furnace was used for the *in situ* observation of inclusion agglomeration. Details of the technique have been published elsewhere.<sup>[17–21]</sup> The steel sample was placed inside a high-purity alumina crucible with an inner diameter of 5.0 mm. The Al<sub>2</sub>O<sub>3</sub> crucible was located at the focal point of a gold-plated ellipsoidal chamber. Before heating, the chamber was filled with pure Ar gas (purity >99.999 pct) under a constant flow of 50 to 60 mL/min and then evacuated to desorb air. The cycle of vacuum and purging with Ar was performed three times to clean the chamber thoroughly. The total time was approximately 30 minutes. The high-purity Ar gas was cleaned by passing the gas through a gas cleaning system to remove moisture and impurity gases. Moreover, thin Ti foil with thickness of 0.0127 mm was wrapped around the upper part of the outer surface of the alumina crucible to prevent reoxidation of the sample surface during heating or cooling. The oxygen partial pressure in the off-gas was between  $3 \times 10^{-19}$  and  $3 \times 10^{-20}$  kPa between 1400 °C and 1600 °C, measured by the oxygen sensor.

The heating profile was first set to 1273 K (1000 °C) with a heating rate of 100 °C/min, subsequently to 1753 K (1480 °C) with a heating rate of 150 °C/min, and to 1793 K (1520 °C) with a heating rate of 10 °C/min. Thereafter, it was raised manually by 0.5 °C to 1 °C every minute. The details of temperature profile can be seen in Figure 1. The temperature was measured using a R-type thermocouple, attached to the bottom of

the Al<sub>2</sub>O<sub>3</sub> crucible. Pure Fe (purity >99.9 pct) was used to calibrate the surface temperature of the sample. The thermocouple temperature on melting was compared with the theoretical melting point of Fe (1811 K (1538 °C)), which was considered as the actual sample surface temperature when pure Fe melted. It was found that the surface temperature of the sample is 30 °C ± 10 °C higher than the thermocouple temperature when pure Fe was melted. This temperature difference was considered throughout the present work.

The inclusion behavior at the metal surface was recorded as a video with maximum 30 frames per second. The magnification 10 times objective lens was mainly used for observing inclusion agglomeration. From the digital video, images were extracted to analyze the distance between inclusions, the inclusion size, and the inclusion shape factor, circularity (CF<sub>k</sub>). The calculation method of CF<sub>k</sub> is expressed as Eq. [1]. The commercial software Image J was used for the measurement. The image frames consisted of 930 × 930 pixels, and one pixel equals 0.47 μm.

$$CF_k = 4\pi \times \frac{A_k}{P_k^2} \quad (k = 1, 2) \quad [1]$$

where CF<sub>k</sub> is defined as circularity and is used to describe the shape factor. CF<sub>k</sub> equals 1 for completely spherical particles. A<sub>k</sub> and P<sub>k</sub> are the area and perimeter of inclusion k, respectively, and are measured by Image J.

An illustration of the calculation of the attractive force based on CLSM video is shown in Figure 2. Equations [2] through [5] show the calculation methods for one inclusion (guest) moving toward a stagnant inclusion 1 (host). A detailed description can be found in

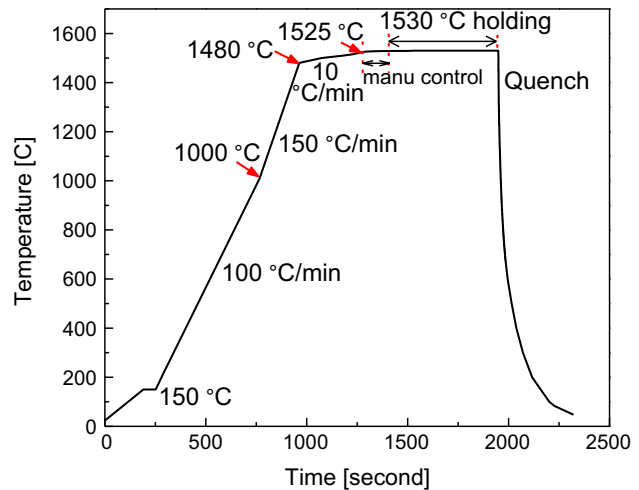


Fig. 1—Temperature profile of *in situ* observation of inclusion agglomeration.

Table I. Chemical Composition of Steel Sample Used in *In-Situ* Observation (Mass Percent)

C	Si	Mn	Ni	Cr	Al	Ti	S	N	O	P	Fe
0.16	0.15	0.84	0.095	0.038	0.01	0.008	0.03	0.016	0.0073	0.012	bal

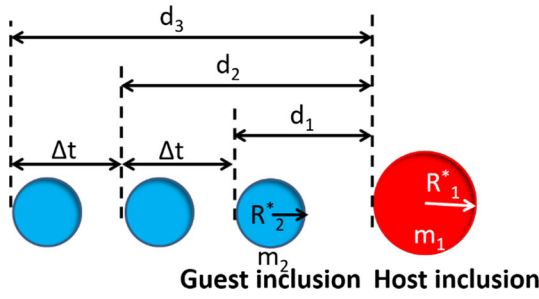


Fig. 2—Schematic illustration to calculate attractive force from CLSM video, adapted from Refs. [8] through [11].

the work of Nakajima and Mizoguchi,<sup>[11]</sup> where  $m_2$  is the mass of the guest inclusion 2 and  $a_i$  is the acceleration of the inclusion pair at each time  $t_i$ . The term  $d_i$  is the distance between two inclusions at each time  $t_i$ . The time interval,  $\Delta t_i$ , equals 0.15 second in this work, and  $R_2$  is the equivalent radius of a circle for inclusion 2. Equivalent radius of a circle is a way to describe the size of an irregular shape inclusion. The radius of a perfect circle, which has the same area as the projected image of the measured inclusion, is used to represent the size of the irregular inclusion. The calculation method is expressed as Eq. [7]. Furthermore, if two inclusions approached each other, a revised parameter of  $m_2/(m_1 + m_2)$  was introduced. In that case, Eq. [6] is used instead of Eq. [5] to calculate the attractive force.

$$a_i = (v_{i+1} - v_i)/\Delta t_i = (d_{i+1}/t_{i+1} - d_i/t_i)\Delta t_i \quad [2]$$

$$\Delta t_i = t_{i+1} - t_i \quad [3]$$

$$m_2 = (4/3) \times \pi \times R_2^* \times R_2^* \times R_2^* \times \rho \quad [4]$$

$$F_{A,i} = m_2 \times a_2 \quad [5]$$

$$F'_{A,i} = m_2 \times a_i \times m_1/(m_1 + m_2) \quad [6]$$

where  $v_i$  is the moving velocity of the inclusion at each time  $i$ .

$$R_k = \sqrt{A_k/\pi} \quad [7]$$

The chemical composition of nonmetallic inclusions in the current steel before and after *in situ* observation was studied using a scanning electron microscope (SEM) (JEOL\* JSM-6610LV) in combination with

\*JEOL is a trademark of Japan Electron Optics Ltd., Tokyo.

energy-dispersive X-ray spectroscopy (EDS). An Oxford Aztec EDS X-ray microanalysis system was used.

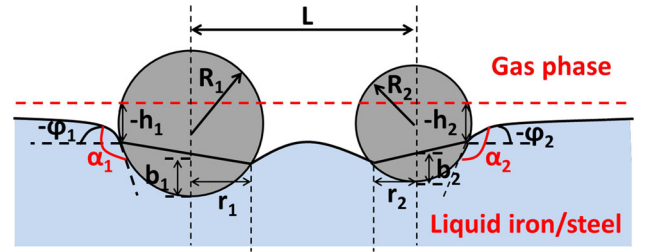


Fig. 3—Schematic illustration of the capillary meniscus around two spherical inclusions, adapted from Refs. [10] through [13].

## B. Theoretical Model for Calculating Attractive Capillary Force

Kralchevsky *et al.*<sup>[16]</sup> developed a mathematical model for the energy and the force balances between two particles floating on the surface of a liquid phase at room temperature. Paunov *et al.*<sup>[17]</sup> reported simplified equations to calculate capillary interaction between two floating particles existing at the gas/liquid interface. Figure 3 shows the force acting on a pair of spherical inclusions with radii  $R_1$  and  $R_2$  floating at the interface between the liquid steel and Ar.<sup>[10–13]</sup>

The capillary interaction energy,  $W$ , between the spherical inclusions is shown as Eq. [8].

$$\Delta W = -\pi\gamma[(Q_1h_1 - Q_{1\infty}h_{1\infty})(1 + O(q^2R_1^2)) + (Q_2h_2 - Q_{2\infty}h_{2\infty})(1 + O(q^2R_2^2))] \quad [8]$$

$$q = \sqrt{\frac{(\rho_{\text{steel}} - \rho_{\text{gas}})g}{\gamma}} \approx \sqrt{\frac{\rho_{\text{steel}}g}{\gamma}}, \text{ where } \rho_{\text{steel}} \gg \rho_{\text{gas}} \quad [9]$$

where  $q$  is the capillary length, defined by Eq. [9].  $\rho_{\text{steel}}$  and  $\rho_{\text{gas}}$  are the densities of liquid steel and gas, respectively;  $\gamma$  is the surface tension of the liquid steel (a value of 1.49 J/m<sup>2</sup><sup>[22]</sup> is used in this study); and  $g$  is gravity acceleration. The subscript  $k$  represents the inclusions 1 and 2 in an inclusion pair. The  $O(x)$  is the zero function of approximation. The capillary charges,  $Q_k$  and  $Q_{k\infty}$ , and the height differences of the meniscus,  $h_k$  and  $h_{k\infty}$ , can be found elsewhere.<sup>[10,11]</sup>

For the different values of  $L$ , the capillary force can be calculated as follows:

$$F = \frac{d(\Delta W)}{dL} \quad [10]$$

The capillary interaction energy between two particles,  $\Delta W$ , can be represented by the contributions of wetting ( $\Delta W_w$ ), meniscus surface tension ( $\Delta W_m$ ), and gravity ( $\Delta W_g$ ). According to this, the following equations can be used for the capillary force. The detailed derivation of the mathematical equations can be found in the work of Kralchevsky *et al.*<sup>[16]</sup> and Paunov *et al.*<sup>[17]</sup>

$$\frac{d\Delta W_w}{dL} = -\pi\gamma \left\{ (qr_1)^2 R_1 \cos\alpha_1 \frac{dh_1}{dL} \times [1 + O(q^2 R_1^2)] + (qr_2)^2 R_2 \cos\alpha_2 \frac{dh_2}{dL} \times [1 + O(q^2 R_2^2)] \right\} \quad [11]$$

$$\frac{d\Delta W_m}{dL} = \pi\gamma \left\{ [Q_1 + (qr_1)^2 R_1 \cos\alpha_1 \frac{dh_1}{dL} \times [1 + O(q^2 R_1^2)]] + [Q_2 + (qr_2)^2 R_2 \cos\alpha_2 \frac{dh_2}{dL} \times [1 + O(q^2 R_2^2)]] \right\} \quad [12]$$

$$\frac{d\Delta W_g}{dL} = -\pi\gamma \left\{ 2Q_1 \frac{dh_1}{dL} [1 + O(q^2 R_1^2)] + 2Q_2 \frac{dh_2}{dL} [1 + O(q^2 R_2^2)] \right\} \quad [13]$$

$$F = -\pi\gamma \left\{ Q_1 \frac{dh_1}{dL} [1 + O(q^2 R_1^2)] + Q_2 \frac{dh_2}{dL} [1 + O(q^2 R_2^2)] \right\} \quad [14]$$

where  $\alpha_1$  and  $\alpha_2$  are contact angles between inclusions 1 and 2 and liquid steel. A measure of 137 deg<sup>[23]</sup> is used for both  $\alpha_1$  and  $\alpha_2$  in this work since inclusions 1 and 2 are  $Al_2O_3$ .

Here, a simplification has been made by Paunov *et al.*<sup>[14]</sup> The following equations have been used:

$$h_1 = h_{1\infty} + Q_j K_0(qL) \quad (r_1 \ll L) \quad [15]$$

$$h_2 = h_{2\infty} + Q_j K_0(qL) \quad (r_2 \ll L) \quad [16]$$

where the function  $K_0(x)$  is the modified Bessel function of zero order.<sup>[24]</sup>

By substituting Eqs. [15] and [16] into Eqs. [14] and [17] can be obtained.

$$F = 2\pi Q_1 Q_2 q K_1(qL) [1 + O(q^2 R_k^2)] \quad (r_k \ll L, k = 1 \text{ or } 2) \quad [17]$$

where  $K_1(x)$  is the modified Bessel function of first order.<sup>[24]</sup> The analogous expression can be seen in Eq. [18]<sup>[24,25]</sup>:

$$K_1(x) = \frac{1}{x} + O(x \ln x) \quad (x \rightarrow 0) \quad [18]$$

By substituting Eq. [18] into Eq. [17], the simplification of calculating the attractive capillary force has been made. Paunov *et al.*<sup>[17]</sup> reported that the final simplified

equation can be expressed as Eq. [19], when the distance between two particles,  $L$ , is between  $r_k$  and  $q^{-1}$ .

$$F = 2\pi\gamma \frac{Q_1 Q_2}{L} \quad (r_k \ll L \ll q^{-1}) \quad [19]$$

$$O(x \ln x) \approx 0 \quad (x \rightarrow 0) \quad [20]$$

The assumption shown in Eq. [20] was used by Paunov *et al.*<sup>[17]</sup> This assumption can be justified from the expression of Eq. [19], although this is not explicitly reported by Paunov *et al.*<sup>[17]</sup>

In this work, another approximation has been made, as shown in Eq. [21]. This is according to the L'Hôpital's rule.<sup>[26]</sup> The following deviations are the modified part in the revised model:

$$\lim_{x \rightarrow 0} (x \ln x) = \lim_{x \rightarrow 0} \left( \frac{\ln x}{1/x} \right) = \lim_{x \rightarrow 0} \frac{(\ln x)'}{(1/x)'} = \lim_{x \rightarrow 0} (-x) \quad [21]$$

According to Eq. [21],  $K_1(qL)$  in Eq. [18] is changed to Eq. [22].

$$K_1(qL) = \frac{1}{qL} + O((qL) \ln(qL)) \approx \frac{1}{qL} - qL \quad (qL \rightarrow 0) \quad [22]$$

Substituting Eq. [22] into Eq. [17], the expression of the capillary force in this work is shown in Eq. [23].

$$F = \frac{2\pi Q_1 Q_2 (1 - q^2 L^2)}{L} \quad (r_k \ll L, k = 1, 2) \quad [23]$$

The comparison between the previous simplification method<sup>[17]</sup> and the present calculation method has been reported in a previous study by the authors.<sup>[27]</sup> According to the model development, the contributions of physical properties, such as surface tension of liquid metal and contact angle between inclusion and liquid metal, are considered in the current capillary force model, see Reference 28. However, the contribution of viscosity of liquid steel in resisting inclusion movement is not considered in the current model. Given the good agreement between the model and the measured data, it would appear that the role of viscosity is negligible, possibly because the inclusions are not deeply immersed in the steel. However, because no variation in viscosity was considered in the current experiments, it is possible that any viscosity effect could be hidden in the zero function of Eqs. [8] and [11] through [14]. It is also worth considering that if the inclusions were situated at the slag/metal interface, the viscosity of slag might well play a more significant role. This is worthy of consideration for future work.

### III. RESULTS AND DISCUSSION

#### A. Observation of $Al_2O_3$ Inclusions Agglomeration at Steel/Ar Gas Interface

The mirror polished steel sample was heated in CLSM, according to the temperature profile in Figure 1. Incipient melting was observed before the sample surface fully

melted. At 1803 K (1530 °C), the  $\delta$ -ferrite grain boundary was melted at first and formed a channel until a large part of the surface was melted. During the incipient melting and initial surface melting, steel melt flow could not be avoided. The inclusions were found to move with the local surface flow. After a short while, surface flow of the melt was inhibited and the steel/Ar interface was almost stagnant. From this stage, the agglomeration process of inclusions was recorded and used to calculate the attractive force. As shown in Table II, the inclusions observed in this study are essentially alumina, titania, and aluminum titanates. There are also MnS inclusions present in the steel, which dissolve during heating. The oxide inclusions observed in the CLSM are pre-existing inclusions that form agglomerates in the liquid phase and grow by collision with other inclusions and agglomerates. Given the stability of these inclusions, there is no significant dissolution. Individual inclusions that form agglomerates sinter at the points of contact.<sup>[29]</sup> Linear aggregates bend under the influence of shear forces in the liquid, folding in on themselves to form more dense spherical aggregates. The forces driving the latter phenomenon will be investigated in detail in a future publication by the authors. Figure 4 shows typical CLSM images for agglomeration of two inclusions of significantly different sizes. The larger size inclusion ( $R > 30 \mu\text{m}$ ) remained stationary and the small size inclusion moved toward the large size inclusion.

*In-situ* observation was terminated when no more inclusions were absorbed by the large size inclusion. The liquid steel was quenched directly from 1803 °k (1530 °C). The CLSM images before and after quenching are shown in Figures 5(a) and (b), respectively, confirming that agglomerated inclusions remained in the same location during quenching. Chemical composition of agglomerated inclusions in the quenched sample was determined by SEM-EDS. Figure 6 shows elemental maps and locations of point analysis of the agglomerated inclusion. The associated EDS compositions of agglomerated inclusions are given in Table II. It was found that the agglomerated inclusion contains mainly  $\text{Al}_2\text{O}_3$ . Besides, Reference 30 reported a phase stability diagram of the Fe-Al-Ti-O system at 1873 K. By using the present steel composition, the stable inclusion phase is predicted as  $\text{Al}_2\text{O}_3$ . In addition, Ti-rich inclusion was detected only in one spot, consisting of a Ti-oxide core and a Ti-Al-O periphery surrounding the core. However, this inclusion type is not considered in this study due to its low concentration.

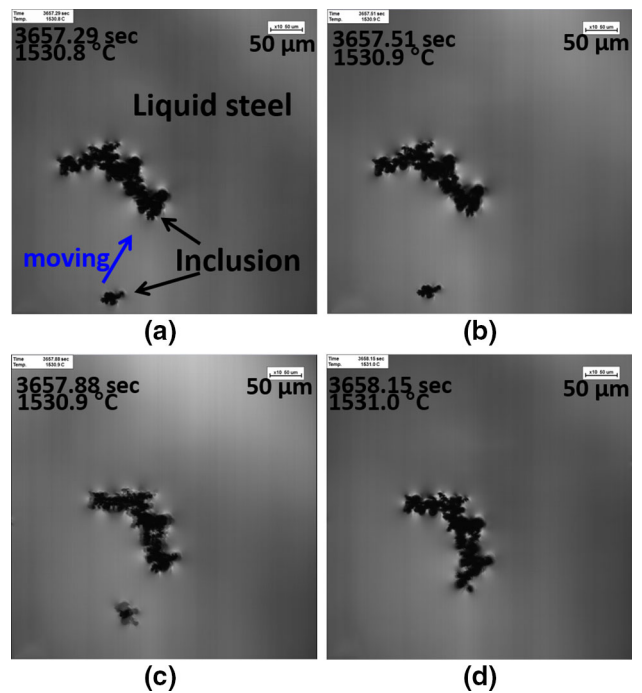


Fig. 4—CLSM images of small size inclusion absorbed by large size inclusion in liquid steel/Ar gas interface.

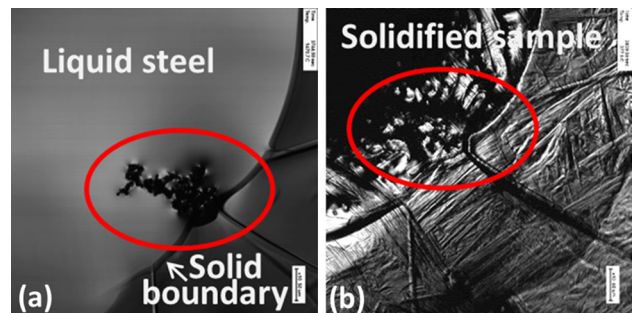


Fig. 5—CLSM images of agglomerated inclusions before and after quenching.

### B. Attractive Force Between $\text{Al}_2\text{O}_3$ Inclusions

By using the images extracted from CLSM videos, the distance between inclusions at different times was measured by Image J software. Figure 7 illustrates the change in the acting distance between inclusions with

Table II. EDS Analysis of Agglomerated Inclusion

Number	Al		Ti		O		Fe	
	Wt Pct	At. Pct	Wt Pct	At. Pct	Wt Pct	At. Pct	Wt Pct	At. Pct
A	5.8	5.4	50.3	26.4	40.6	63.8	1.5	0.7
B	37.4	29.6	6.8	3.0	43.6	58.1	6.7	2.6
C	20.8	16.0	22.5	9.8	52.3	68.2	1.2	0.4
D	50.0	37.5	0.8	0.3	43.9	55.6	2.0	0.7
E	51.2	28.9	—	—	43.3	55.4	2.9	1.0
F	45.1	32.9	0.9	0.4	48.4	59.5	1.4	0.5
G	44.2	32.1	0.6	0.2	49.4	60.4	—	—

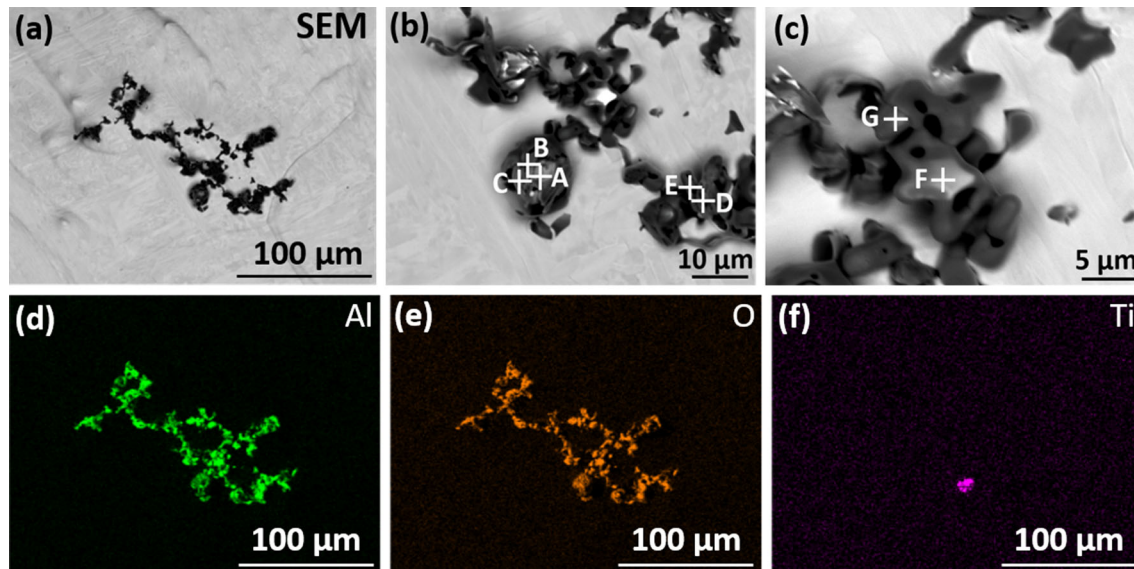


Fig. 6—SEM-EDS elemental mapping of agglomerated inclusions after *in situ* observation experiments: (a) morphology of the agglomerated inclusion; (b) and (c) schematic locations of EDS point analysis; and (d) through (f) elemental mapping of Al, O, and Ti, respectively.

respect to time and radii of inclusions. The terms  $R_1$  and  $R_2$  represent the radii of different  $\text{Al}_2\text{O}_3$  inclusions. It is found that the distance between small and large size  $\text{Al}_2\text{O}_3$  inclusions decreases as time progresses.

The velocity and acceleration of inclusions were calculated in order to confirm agglomeration between inclusions caused by attraction, rather than by flow of the steel. These parameters were plotted with respect to the distance between inclusions, as shown in Figures 8(a) and (b), respectively. It is found that both the velocity and acceleration of small size inclusions moving toward the large size inclusion are increased as distance decreases. This indicates that the agglomeration is caused by the attraction of the small size inclusions toward the large size inclusion. If the inclusion was under the influence of liquid steel flow, the velocity would be constant and the acceleration should be zero. This finding was further confirmed by the observation of the attraction of small size inclusions by the large size inclusion occurring in different directions.

The attractive force was calculated by using Eqs. [2] through [6]. The relationship between distance and attractive force is shown in Figure 9. The attractive forces are mainly varied from  $1 \times 10^{-17}$  to  $1 \times 10^{-11}$  N. It is found that attractive force increases as the distance between inclusions decreases. In addition, a very small amount of  $\text{TiAlO}_x$  inclusion was found (SEM-EDS images in Figure 6). Actually, it is observed that relatively small size  $\text{TiAlO}_x$  inclusion was absorbed by the large size  $\text{Al}_2\text{O}_3$  inclusion. Thereafter, the attractive force between this inclusion pair is calculated using the same method presented in this work, and the attraction force is smaller than the force between  $\text{Al}_2\text{O}_3$  inclusion pairs. However, the amount of  $\text{TiAlO}_x$  inclusion is insufficient to make a comparison of agglomeration behavior between  $\text{Al}_2\text{O}_3$  and  $\text{TiAlO}_x$ . More work will be considered in the future work.

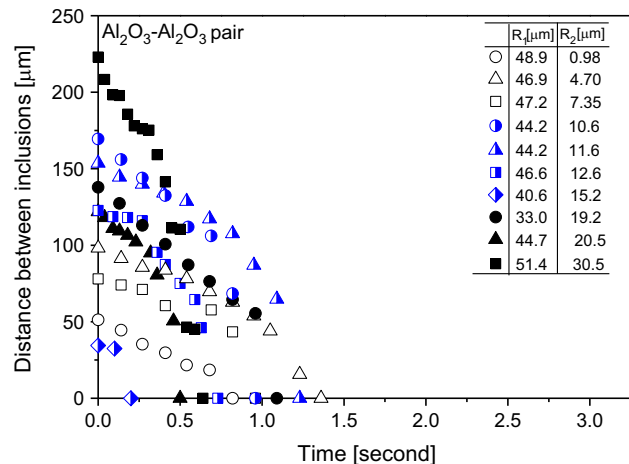


Fig. 7—Change in distance between inclusions with respect to time and radii of inclusions.

The attractive force of  $\text{Al}_2\text{O}_3$  inclusion pairs increased as the size of small size inclusion increased. This finding is consistent with the literature.<sup>[8]</sup> In a previous study by Yin *et al.*,<sup>[8]</sup> the radius of the large inclusion was less than  $30 \mu\text{m}$  and the radius of the small inclusion varied from  $2.5$  to  $10 \mu\text{m}$ . In their case, the maximum attractive force was up to  $1 \times 10^{-14}$ , which is smaller than the maximum force of  $1 \times 10^{-11}$  N calculated in this study. This is certainly due to the difference in size range of inclusions.

Besides the attractive force, it is seen that the distance at which a small size  $\text{Al}_2\text{O}_3$  inclusion starts to be attracted by a large size  $\text{Al}_2\text{O}_3$  inclusion increases with increasing inclusion size ( $R_l$ ). In all subsequent discussion, this distance is termed acting distance. Yin *et al.*<sup>[8]</sup> reported that the acting distance increases as the size of the larger inclusion in an inclusion pair increases. In the

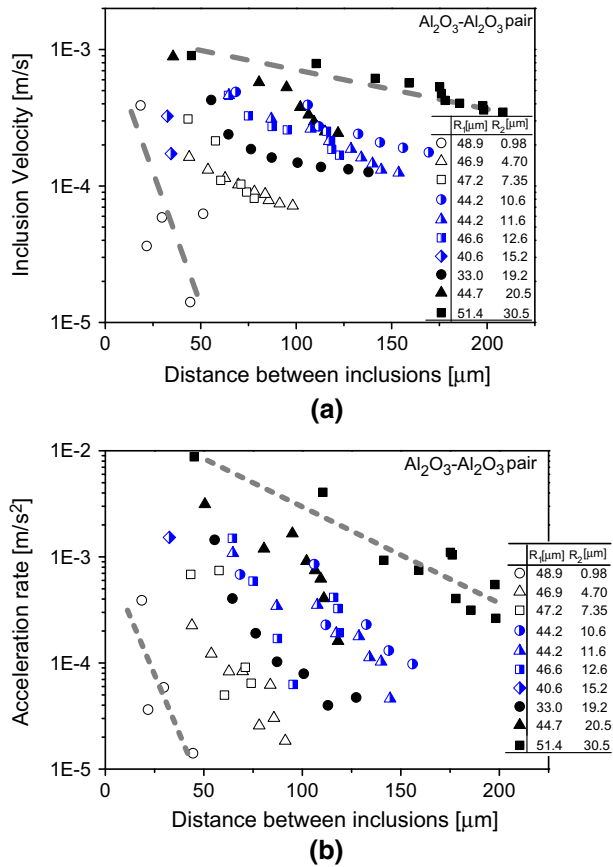


Fig. 8—Relationship between distance and (a) velocity and (b) acceleration of the inclusion pair.

current study, the size of the large inclusion remains almost constant and that of the small inclusion varies. Combining the current study and the previous finding by Yin *et al.*<sup>[8]</sup> shows that the acting distance for inclusion agglomeration can increase with increasing size of either the small or large inclusion. It is also important to note that the acting distance in this work is larger than that reported previously<sup>[8,9]</sup> because of the larger inclusion size considered here.

### C. Validation of Model

Yin *et al.*<sup>[8,9]</sup> reported that the inclusion is partially immersed at the steel/Ar interface and the peripheral surface of liquid steel depressed around the inclusion according to the force balance between gravity, buoyancy, and interfacial tension forces acting on the inclusion. When two inclusions are very close, the liquid steel surface between two inclusions will be further depressed. This leads to a difference of the capillary pressure between the outside and inside of the inclusion pair. The difference of capillary pressure will push the inclusions toward each other. Subsequently, Nakajima and co-workers<sup>[10,11]</sup> and Jönsson and co-workers<sup>[12,13]</sup> claimed that the capillary force is the key reason for inclusion agglomeration at steel/Ar and steel/slag interfaces.

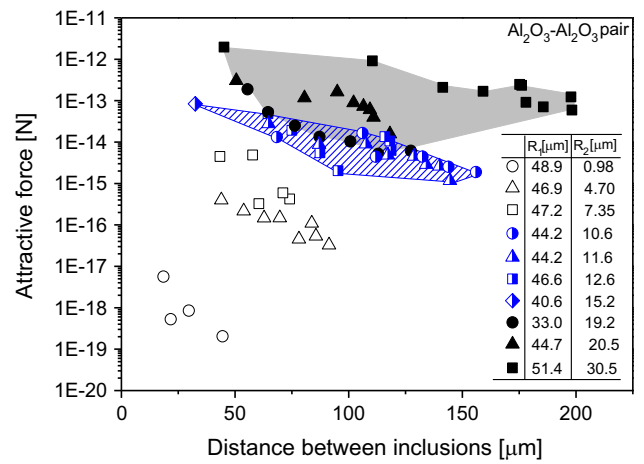


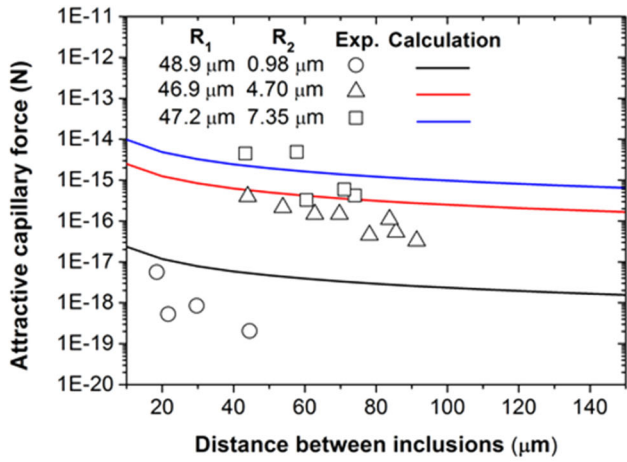
Fig. 9—Comparison of attractive forces between inclusion pairs with respect to distance between inclusions and their size ratio.

In this work, a revision to the Paunov simplified model has been made. The comparison of capillary forces calculated using the revised Paunov simplified model with experimental results obtained in this study is provided in Figure 10. Figures 10(a) through (c) show the calculation results for attractive capillary forces using equivalent radius of a circle,  $R_k$  ( $k = 1, 2$ ), whereas Figures 10(d) through (f) show the calculation results for those using effective radius of inclusion,  $R_{k,eff}$  ( $k = 1, 2$ ). Previous studies<sup>[11,13]</sup> imply that the application of equivalent radius  $R_k$  to the inclusions with the lower degree of circularity will cause serious error for the calculation of capillary force. In this case, the effective radius,  $R_{k,eff}$ , is introduced based on the perimeter of the inclusion,  $P_k$ , from Eqs. [1] through [7]. The calculation method of  $R_{k,eff}$  is shown in Eq. [24], where circularity,  $CF_k$ , is used.

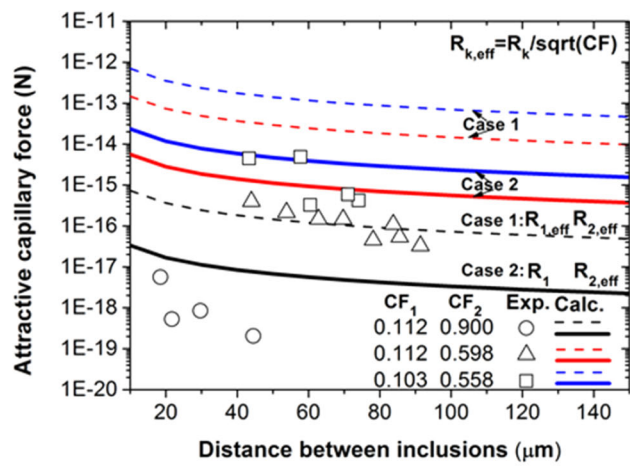
$$R_{k,eff} = P_k / 2\pi = R_k / \sqrt{CF_k} \quad [24]$$

It is seen that the calculation results using  $R_k$  offer a reasonable fit to almost all the experimental data. The only exception is when  $R_2$  equals  $0.98 \mu\text{m}$ . Besides, the dash lines (case 1) in Figures 10(d) through (f) represent the calculation results using  $R_{1,eff}$  and  $R_{2,eff}$ . However, it is shown that all the calculation results deviate from the present data. This is most likely because the size of inclusion 1 in the present experiment is quite large, mainly larger than  $44 \mu\text{m}$ , and its circularity factor is quite small, mainly less than 0.15. However, the inclusions in previous studies,<sup>[11,13]</sup> which use  $R_{k,eff}$  in the calculations, typically have much smaller size ( $<20 \mu\text{m}$ ) or much larger circularity ( $\sim 0.8$ ).

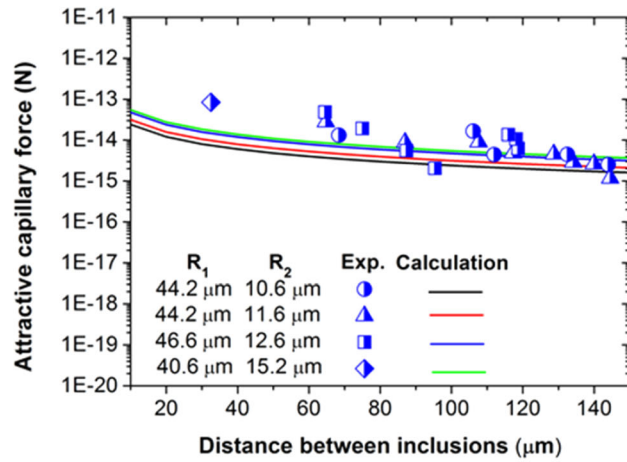
In order to know if this consideration is correct, the calculations of case 2, which use equivalent radius for inclusion 1 ( $R_1$ ) and effective radius for inclusion 2 ( $R_{2,eff}$ ), are performed (see the thick solid lines in Figures 10(d) through (f)). Compared with the calculations using equivalent radius in Figures 10(a) through (c), the calculations of case 2 when  $R_2$  equals 7.35, 15.2, 20.5, and  $30.5 \mu\text{m}$  are closer to experimental data. The remaining fittings using case 2 are similar or even worse,



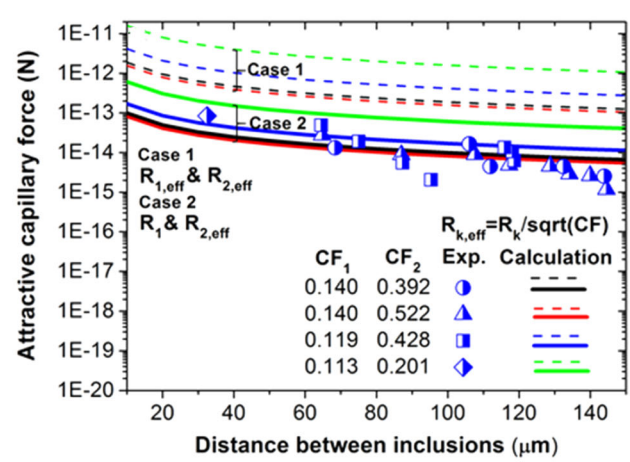
(a)



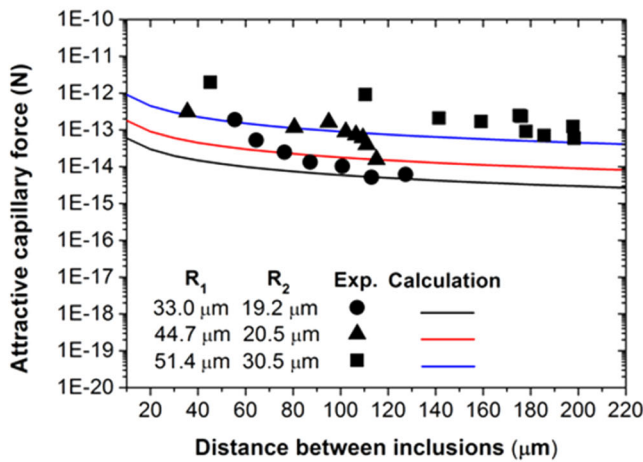
(d)



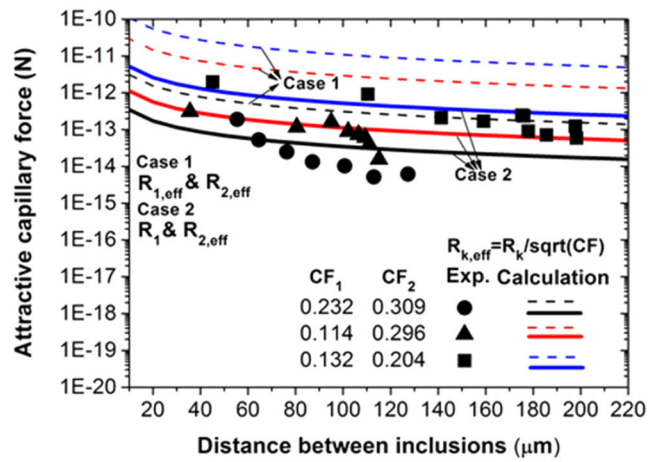
(b)



(e)



(c)



(f)

Fig. 10—Relationship between distance and attractive force: (a) through (c) results using equivalent radius of a circle, and (d) through (f) results using effective radius for the dotted lines, and for the thick solid lines used equivalent radius for the larger inclusion and effective radius for the smaller inclusion.

compared with the results in Figures 10(a) through (c). In this case, it is concluded that the model calculation using equivalent radius of inclusions is closer to the

present experimental data because of the inclusion characteristics. Compared with the present calculations and previous results,<sup>[11,13]</sup> it appears that the use of



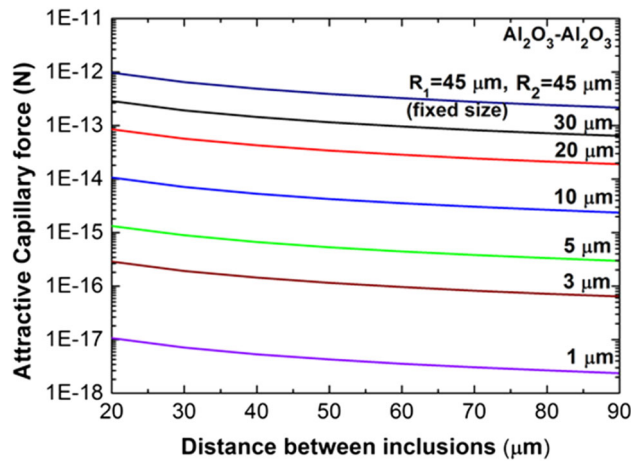


Fig. 11—Effect of inclusion size on attractive capillary force, where the surface tension of steel ( $\gamma_{\text{steel}}$ ) equals  $1.49 \text{ J/m}^2$ , density of inclusion ( $\rho_{\text{inclusion}}$ ) equals  $3950 \text{ kg/m}^3$ , and the contact angle is between  $\text{Al}_2\text{O}_3$  and steel ( $\alpha_1$  and  $\alpha_2$ ).

equivalent radius for inclusions with large size and low circularity (cluster) whereas the use of effective radius for inclusions with small size or high circularity in model development can offer a better agreement with attractive capillary force between inclusions.

#### D. Effect of Inclusion Size

In order to investigate the effect of inclusion size on the attractive force, the revised model was used to calculate the capillary force of inclusions with various sizes. In this calculation,  $3950 \text{ kg/m}^3$  is used as the density of  $\text{Al}_2\text{O}_3$ ,  $7000 \text{ kg/m}^3$  is used as the density of liquid steel, and  $137 \text{ deg}$  is used as the contact angle between  $\text{Al}_2\text{O}_3$  inclusion and liquid steel. To maintain consistency with experimental observations, the radius of the large size inclusion,  $R_1$ , was fixed as  $45 \text{ }\mu\text{m}$ , which is the average radius of inclusion 1 in experiments. The radius of the small inclusion,  $R_2$ , was varied from  $1$  to  $45 \text{ }\mu\text{m}$ . The results are shown in Figure 11.

Figure 11 shows that the attractive capillary force increases as the distance between inclusions decreases regardless of the radius of small inclusion  $R_2$ . When the distance decreases from  $90$  to  $20 \text{ }\mu\text{m}$ , the attractive capillary force increases around one order of magnitude in each size group. Based on the model description in Section II, it is known that the attractive force is inversely proportional to the distance between inclusions. A decrease in distance leads to an increase in the difference of liquid surface height ( $\Delta h$ ) between and outside agglomerated inclusions. Moreover, it is found that the attractive capillary force increases by several orders of magnitude with an increase in  $R_2$  from  $1$  to  $45 \text{ }\mu\text{m}$ . For example, the attractive capillary force is between  $1 \times 10^{-18}$  and  $1 \times 10^{-17} \text{ N}$  when  $R_2$  is  $1 \text{ }\mu\text{m}$ . It increases up to  $1 \times 10^{-12} \text{ N}$  for  $45 \text{ }\mu\text{m}$  of  $R_2$ . This finding indicates that stronger attraction exists between larger size inclusions.

CLSM video shows that once the larger size inclusion forms, all of the small size inclusions are directly

attracted by the large size inclusion. Agglomeration between small size inclusions is occasionally observed. From this phenomenon, it can be concluded that the attraction of the small size inclusion by the large size inclusion plays a more important role in the formation of much larger size inclusions (clusters) compared to the attraction between small size inclusions. In Figure 8, it is clear that the inclusion moving velocity and acceleration increase with increasing inclusion size. The agglomeration speed would be accelerated once large inclusion clusters form from single inclusions.

## IV. CONCLUSIONS

The agglomeration behavior of alumina inclusions at the steel/Ar interface was investigated by *in situ* observation experiments and the attractive capillary force model. The obtained conclusions are summarized as follows.

1. It is found that larger size  $\text{Al}_2\text{O}_3$  inclusions are more readily attracted at the steel/Ar interface. This has been affirmed by the previous experimental data; however, the present experimental work offers the results with a wider size range of inclusions. Moreover, the revised capillary force demonstrates that larger inclusions are more strongly attracted.
2. The revised capillary force model offers a reasonable fit with the present experimental data for different inclusion sizes. Thus, this model can be used for quantitative evaluation of agglomeration of inclusions with a wide size range at the steel/Ar interface.
3. For inclusion pairs where the large inclusion is greater than  $40 \text{ }\mu\text{m}$  with circularity less than  $0.2$  and the small inclusion is between  $4.7$  and  $30 \text{ }\mu\text{m}$  with circularity greater than  $0.2$ , the model offers the best fit to experimental data when the equivalent radius is used for the large inclusion and the effective radius is used for the small inclusion. More work is required to evaluate the applicability of these criteria over a wider range of inclusion sizes and shapes.

## ACKNOWLEDGMENTS

The authors thank the Natural Sciences and Engineering Research Council of Canada (NSERC), the Canada Foundation for Innovation John Evans Leaders Fund (CFI JELF, Project No. 32826), and the McMaster Steel Research Centre (SRC) members for funding the research. Professor Keiji Nakajima (KTH Royal Institute of Technology) is also acknowledged by one of the authors (WM) for introducing the agglomeration experiment. Dr. Hongbin Yin (ArcelorMittal, Global R&D) is acknowledged by the authors for discussing the details of *in situ* observation experiments using CLSM. The Canadian Centre for Electron Microscopy (CCEM), McMaster University, is also acknowledged for the support of characterization.

## REFERENCES

1. T.A. Engh: *Principles of Metals Refining*, Oxford University Press, New York, NY, 1992, pp. 1–3.
2. L. Zhang and B.G. Thomas: *ISIJ Int.*, 2003, vol. 43, pp. 271–91.
3. O. Wijk: *Proc. 7th Int. Conf. Refining Process (SCANINJECT VII)*, Luleå, Sweden, 1995, pp. 35–67.
4. Y. Sahai and T. Emi: *Tundish Technology for Clean Steel Production*, World Scientific Publishing Co. Pte. Ltd., pp. 292–94.
5. S. Taniguchi and A. Kikuchi: *Testu-to-Hagané*, 1992, vol. 78, pp. 527–35.
6. Y. Miki, H. Kitaoka, T. Sakuraya, and T. Fuji: *Testu-to-Hagané*, 1992, vol. 78, pp. 431–38.
7. K. Nakanishi and J. Szekely: *Trans. ISIJ*, 1975, vol. 15, pp. 522–30.
8. H.B. Yin, H. Shibata, T. Emi, and M. Suzuki: *ISIJ Int.*, 1997, vol. 37, pp. 936–45.
9. H.B. Yin, H. Shibata, T. Emi, and M. Suzuki: *ISIJ Int.*, 1997, vol. 37, pp. 946–55.
10. S. Kimura, K. Nakajima, and S. Mizoguchi: *Metall. Mater. Trans. B*, 2001, vol. 32B, pp. 79–85.
11. K. Nakajima and S. Mizoguchi: *Metall. Mater. Trans. B*, 2001, vol. 32B, pp. 629–41.
12. J. Appelberg, K. Nakajima, H. Shibata, A. Tilliander, and P. Jönsson: *Mater. Sci. Eng., A*, 2008, vol. 495, pp. 330–34.
13. J. Wikström, K. Nakajima, H. Shibata, A. Tilliander, and P. Jönsson: *Ironmaking Steelmaking*, 2008, vol. 35, pp. 589–99.
14. Y. Kang, B. Sahebkar, P.R. Scheller, K. Morita, and D. Sichen: *Metall. Mater. Trans. B*, 2011, vol. 42B, pp. 522–34.
15. G. Du, J. Li, Z.B. Wang, and C.B. Shi: *Steel Res. Int.*, 2017, vol. 88, art. no. 1600185.
16. P.A. Kralchevsky, V.N. Paunov, N.D. Denkov, I.B.V. Ivanov, and K. Nagayama: *J. Coll. Interface Sci.*, 1993, vol. 155, pp. 420–37.
17. V.N. Paunov, P.A. Kralchevsky, N.D. Denkov, and K. Nagayama: *J. Coll. Interface Sci.*, 1993, vol. 157, pp. 100–12.
18. H. Chikama, H. Shibata, T. Emi, and M. Suzuki: *Mater. Trans., JIM*, 1996, vol. 37, pp. 620–26.
19. J. Monaghan and L. Chen: *J. Non-Crystalline Solids*, 2004, vol. 347, pp. 254–61.
20. W. Mu, H. Shibata, P. Hedström, P.G. Jönsson, and K. Nakajima: *Metall. Mater. Trans. B*, 2016, vol. 47B, pp. 2133–47.
21. W. Mu, P.G. Jönsson, and K. Nakajima: *J. Mater. Sci.*, 2016, vol. 51, pp. 2168–80.
22. C. Xuan, H. Shibata, S. Sukenaga, P.G. Jönsson, and K. Nakajima: *ISIJ Int.*, 2015, vol. 55, pp. 1882–90.
23. K. Ogino, K. Nogi, and Y. Koshida: *Tetsu-to-Hagané*, 1973, vol. 59, pp. 1380–87.
24. E. Jahnke, F. Emde, and F. Lösch: *Tables of Higher Functions*, McGraw-Hill, New York, NY, 1960.
25. M. Abramovitz and I.A. Stegun: *Handbook of Mathematical Functions*, Dover, New York, NY, 1965.
26. C.F. Chan Man Fong, D. De Kee, and P.N. Kaloni: *Advanced Mathematics for Engineering and Science*, World Scientific Publishing Co. Pte. Ltd., 2003, p. 5.
27. W. Mu, N. Dogan, and K.S. Coley: *5th Int. Conf. on Process Development in Iron and Steelmaking (SCANMET V)*, Luleå, June 12–15, 2016, CD-Rom.
28. W. Mu, N. Dogan, and K.S. Coley: *Metall. Mater. Trans. B*, 2017, vol. 48, pp. 2092–103.
29. K. Sasai and Y. Mizukami: *ISIJ Int.*, 2001, vol. 41, pp. 1331–39.
30. C. Xuan, W. Mu, Z.I. Olano, P.G. Jönsson, and K. Nakajima: *Steel Res. Int.*, 2016, vol. 87, pp. 911–20.